THEORY AND COMPARISON WITH TESTS OF TWO FULL–SCALE PROPROTORS

Wayne Johnson
Research Scientist
Large-Scale Aerodynamics Branch
Ames Research Center, NASA
and
U.S. Army Air Mobility R & D Laboratory
Moffett Field, California

Abstract

A nine degrees-of-freedom theoretical model has been developed for investigations of the dynamics of a proprotor operating in high inflow axial flight on a cantilever wing. The theory is described, and the results of the analysis are presented for two proprotor configurations: a gimballed, stiff-inplane rotor, and a hingeless, soft-inplane rotor. The influence of various elements of the theory is discussed, including the modeling used for the blade and wing aerodynamics and the influence of the rotor lag degree of freedom. The results from full-scale tests of these two proprotors are presented and compared with the theoretical results.

Notation

c_{ℓ_α}	blade lift-curve slope
p	wing torsion degree of freedom
q_1	wing vertical bending degree of freedom
q_2	wing chordwise bending degree of freedom
R	rotor radius
V	forward velocity
β	blade flap degree of freedom
β_0	rotor coning degree of freedom
β_{1c}	rotor tip path plane pitch degree of freedom
β_{1s}	rotor tip path plane yaw degree of freedom
γ	blade Lock number
δ_3	pitch/flap coupling
ζ	damping ratio of eigenvalue, $-\text{Re}\lambda/\lvert\lambda\rvert$
ζ	blade lag degree of freedom
ζ_0	rotor collective lag degree of freedom
$\dot{\zeta}_0$	time derivative of ζ_0; rotor speed perturbation degree of freedom for autorotation case
ζ_{1c}	rotor vertical cyclic lag degree of freedom
ζ_{1s}	rotor lateral cyclic lag degree of freedom
λ	eigenvalue or root
ν_β	rotating natural frequency of blade flap motion
ν_ζ	rotating natural frequency of blade lag motion
ω	frequency of eigenvalue, $\text{Im}\lambda$
Ω	rotor rotational speed

The tilting proprotor aircraft is a promising concept for short haul, V/STOL missions. This aircraft uses low disk loading rotors located on the wing tips to provide lift and control in hover and low speed flight; it also uses the same rotors to provide propulsive force in high speed cruise, the lift then being supplied by a conventional wing. Such operation requires a ninety degree change in the rotor thrust direction, which is accomplished by mechanically tilting the rotor shaft axis. Thus the aircraft combines the efficient VTOL capability of the helicopter with the efficient, high speed cruise capability of a turboprop aircraft. With the flexible blades of low disk loading rotors, the blade motion is as important an aspect of tilt rotor dynamics as it is for helicopters. When operated in cruise mode (axial flight at high forward speed), the rotor is operating at a high inflow ratio (the ratio of axial velocity to the rotor tip speed); such operation introduces aerodynamic phenomena not encountered with the helicopter rotor, which is characterized by low inflow. The combination of flapping rotors operating at a high inflow ratio on the tips of flexible wings leads to dynamic and aerodynamic characteristics that are in many ways unique to this configuration. The combination of efficient VTOL and high speed cruise capabilities is very attractive; it is therefore important to establish a clear understanding of the behavior of this aircraft and adequate methods to predict it, to enable a confident design of the aircraft. Experimental and theoretical investigations have been conducted over several years to provide this capability. However, much remains to be studied, both in the fundamental behavior and in the more sophisticated areas such as the design and development of automatic control systems for the vehicle. This paper presents the results of a theoretical model for a proprotor on a cantilever wing, including application to two proprotor designs: a gimballed, stiff-inplane rotor and a hingeless, soft-inplane rotor. Using these two cases, the influence on the system dynamics of several elements of the analysis was examined, including the effects of the rotor blade lag motion and the rotor and wing aerodynamic models. The predicted stability characteristics are then compared with the results of full-scale tests of these two proprotor designs. The development of this theory is presented in detail in Reference 1, together with some additional applications to the analysis of proprotor aeroelastic behavior.

Analytical Model

Figure 1 shows the proprotor configuration considered for the theory and for the full-scale tests. The rotor is operating in high inflow axial flight on a cantilever wing. For the tests, the rotor was unpowered, hence operating in autorotation (really in the windmill brake state). This configuration incorporates the features of greatest importance to the aircraft: the high inflow aerodynamics of a flapping rotor in axial flow and the coupled dynamics of the rotor/pylon/wing aeroelastic system. Many features of the aircraft-coupled wing and rotor motion may be studied with such a model, theoretically and experimentally, with the understanding that the model must eventually incorporate the entire aircraft.

159

The theoretical model of the proprotor developed in Reference 1 consists of nine degrees of freedom: the first mode flap (out of disk plane) and lag (inplane) motion for each of three blades; and vertical bending, chordwise bending, and torsion for the cantilever wing. The degrees of freedom of the individual rotor blades are combined into degrees of freedom representing the motion of the rotor as a whole in the nonrotating frame. Thus the rotor flap motion is represented by tip path plane pitch and yaw (β_{1c} and β_{1s}) and coning (β_0) degrees of freedom. The rotor lag motion is represented by cyclic lag ζ_{1c} and ζ_{1s} (lateral and vertical shift of the rotor net center of gravity) and collective lag ζ_0. Wing vertical and chordwise bending of the elastic axis (q_1 and q_2) and torsion about the elastic axis (p) complete the set of nine degrees of freedom.

The rotor blade motion is represented by first mode flap and lag motion, which are assumed to be respectively pure out-of-plane and pure inplane deflection of the blade spar. For the gimballed and hingeless rotor blades considered here (except for the flap mode of the gimballed rotor), there is, in fact, some elastic coupling of the flap and lag modes, so that there is actually participation of both out-of-plane and inplane motion in each mode. In the coefficients giving the aerodynamic forces on the rotor, it is further assumed that the mode shapes are proportional to the radial distance from the hub, i.e., equivalent to rigid body rotation about a central hinge. The model based on these two assumptions, which considerably simplify the aerodynamic and structural terms of the rotor equations, proves to be an adequate representation of the proprotor dynamics.

The theoretical results presented here will usually be for the rotor operating unpowered, i.e., windmilling or autorotation operation. An important element of autorotation dynamic behavior is the rotor speed perturbation. With no restraint of the rotor shaft rotation, this degree of freedom has considerable influence on the aeroelastic behavior of the proprotor and wing. The rotor speed perturbation is modeled by using the collective lag mode ζ_0. By setting the rotating natural frequency of this mode to zero, i.e., zero spring restraint, ζ_0 becomes equivalent to the rotor speed perturbation. (The natural frequency for the cyclic lag modes, ζ_{1c} and ζ_{1s}, is not set to zero in the representation.) The other extreme case is that of the hub operating at constant angular velocity (Ω) with no speed perturbation, with ζ_0 then the elastic inplane deflection of the blade with respect to the ʻhub. This case will be considered to represent powered operation of the rotor, although it is really the limit of operation with a perfect governor on rotor speed.

The proprotor operating in high inflow has simpler aerodynamics than the low inflow rotor in forward flight. As for the case of low inflow (i.e., the hovering helicopter rotor), the symmetry of axial flow results in a corresponding symmetry in the equations of motion; it also means that the differential equations of motion have constant coefficients. In high inflow there is the additional fact that both out-of-plane and inplane motions of the blade produce significant angle-of-attack changes at the sections, and the resulting lift increment has significant components both normal to and in the disk plane. Hence the rotor aerodynamic forces are primarily due to the lift changes produced by angle-of-attack changes, i.e., the c_{ℓ_α} terms in the aerodynamic coefficients. This is in contrast to low inflow, where, for example, the inplane blade motion produces significant contributions to the forces by the lift and drag increments

due to the dynamic pressure changes, i.e., the c_ℓ and c_d terms in the aerodynamic coefficients. As a result, high inflow rotor aerodynamics are well represented by considering only the c_{ℓ_α} forces. If, in addition, the lift curve slope is assumed constant, then the aerodynamic coefficients depend on only two parameters, the Lock number γ and the inflow ratio $V/\Omega R$. Reference 1 presents the aerodynamic coefficients also for a more complete theoretical model of the rotor aerodynamics, namely a perturbation about the local trim state, including the c_{ℓ_α}, c_ℓ, c_d, and c_{d_α} terms (and also derivatives with respect to the Mach number). Such a model is in fact little more difficult to derive than with the c_{ℓ_α} terms alone. The influence of its use in the theory is examined below.

This nine degrees-of-freedom model will have nine roots or eigenvalues (really nine pairs of complex roots) and correspondingly nine eigenvectors or modes. Of course, each mode involves motion of all nine degrees of freedom. The modes are identifiable by their frequencies (which will be near the uncoupled natural frequencies, nonrotating for the rotor modes), and also by the participation of the degrees of freedom in the eigenvector. The nine modes will be denoted as follows (the approximate uncoupled, nonrotating natural frequency of the mode is given in parentheses):

p	wing torsion (ω_p)
q_1	wing vertical bending (ω_{q_1})
q_2	wing chordwise bending (ω_{q_2})
β	coning (ν_β)
$\beta + 1$	high frequency flap ($\nu_\beta + \Omega$)
$\beta - 1$	low-frequency flap ($\nu_\beta - \Omega$)
ζ	collective lag (ν_ζ)
$\zeta + 1$	high-frequency lag ($\nu_\zeta + \Omega$)
$\zeta - 1$	low-frequency lag ($\nu_\zeta - \Omega$)

The basic theoretical model will consist of all nine degrees of freedom, autorotation operation, and just the c_{ℓ_α} rotor aerodynamic forces. The wing aerodynamic forces are also included (based on a strip theory calculation). The dynamic stability of the system, specifically the frequency and damping ratio of the modes, will be examined for variations of the forward velocity V and the rotor rotational speed Ω. Both V and Ω sweeps change the inflow ratio $V/\Omega R$, and hence the rotor and wing aerodynamic forces. A variation of the rotor speed Ω also changes the values of the wing and rotor blade nondimensional (per rev) natural frequencies. The rotor frequencies may also vary with $V/\Omega R$ due to the change in the rotor collective pitch angle. Several elements of the theoretical model will be examined to determine their influence on the predicted proprotor dynamics: the influence of the blade lag motion (by dropping the ζ_{1c} and ζ_{1s} degrees of freedom), the wing aerodynamics (by dropping the wing aerodynamic coefficients), the rotor speed perturbation (i.e., the autorotation and powered cases), and the more complete model of the rotor aerodynamics (compared to just the c_{ℓ_α} terms).

Two Full-Scale Proprotors

The theory described above will be applied to two full-scale proprotors. The first is a 25-ft diameter gimballed, stiff-inplane proprotor, designed and constructed by the Bell Helicopter Company, and tested in the Ames 40- by 80-ft wind tunnel in July 1970. The second is a 26-ft diameter hingeless, soft-inplane

160

proprotor, designed and constructed by the Boeing Vertol Company, and tested in the Ames 40- by 80-ft wind tunnel in August 1972. The configuration for the dynamics tests consisted of the windmilling rotor operating in high inflow axial flow on the tip of a cantilever wing, as shown in figure 1. As far as their dynamic characteristics are concerned, the two rotors differ primarily in the placement of the rotating natural frequencies of the blade flap and lag motions. The Bell rotor has a gimballed hub and stiff-inplane cantilever blade attachment to the hub, hence $\nu_\beta = 1/\text{rev}$ (nearly, for it does have a weak hub spring) and $\nu_\zeta > 1/\text{rev}$; it also incorporates positive pitch/flap coupling ($\delta_3 < 0$) to increase the blade flap/lag stability. The Boeing rotor has a cantilever or hingeless hub with soft-inplane blade attachment, hence $\nu_\beta > 1/\text{rev}$ and $\nu_\zeta < 1/\text{rev}$. The different placement of the blade frequencies, at the opposing extremes of the possible choices, results in quite different dynamic characteristics for the two aircraft.

The rotors are described in References 2 to 5. Table I gives the major parameters of the rotor, and of the cantilever wing used in the full-scale tests (a more complete description of the parameters required by the theory is given in Reference 1). The wing frequencies in the theory were match to the experimentally measured values by adjusting the spring constants. The typical wing frequencies given in table I are for the coupled motion of the system (including the rotor) at 100 knots and design Ω. The blade rotating natural frequencies are shown in figures 2 and 3 for the Bell and Boeing rotors, respectively. The variation of the Bell lag frequency (fig. 2b) with $V/\Omega R$ is due to the collective pitch change. The Boeing rotor blade frequencies vary little with collective pitch ($V/\Omega R$) since the blade has nearly isotropic stiffness at the root.

The damping ratio of the wing modes was measured in the full-scale tests by the following technique. The wing motion was excited by oscillating an aerodynamic shaker vane on the wing tip (visible in fig. 1) at the wing natural frequency. After a sufficient amplitude was achieved, the vane was stopped. Then the frequency and damping ratio were determined from the decay of the subsequent transient motion of the wing.

Results and Discussion

Gimballed, Stiff-Inplane Rotor

The effects of several elements of the theoretical model will be examined for a gimballed, stiff-inplane rotor (the Bell rotor). The theoretical results will then be compared with the results of full-scale tests. The test results and results from the Bell theories are from Reference 2. The predicted variation of the system stability with forward speed V at the normal airplane mode rotor speed ($\Omega = 458$ rpm) is shown in figure 4, in terms of the frequency and damping ratio of the eigenvalues. The wing vertical bending mode (q_1) becomes unstable at 495 knots. The damping of that mode first increases with speed; the peak is due to coupling between the wing vertical bending (q_1) and low-frequency rotor lag ($\zeta - 1$) modes (it occurs at the resonance of the frequencies of these two modes). Figure 5 shows the influence of the rotor lag motion, comparing the damping of the wing modes with and without the ζ_{1c} and ζ_{1s} degrees of freedom. The rotor low-frequency lag mode has an important influence on the motion, particularly on the wing vertical bending mode; the q_1 damping is increased when its frequency is below that of the

$\zeta - 1$ mode (low V), and decreased when its frequency is above that value. The high speed instability is relatively unaffected, however, indicating that the mechanism of that instability involves primarily the rotor flap motion. Therefore, the net effect of the reduced damping at high speed due to the lag motion is a reduction of the rate at which the damping decreases, which is beneficial since the instability is then less severe.

Figure 6 shows the influence of powered operation (stabilizing) and of omitting the wing aerodynamics (destabilizing). The powered state effect is the influence of dropping the rotor speed perturbation degree of freedom. The wing aerodynamics effect is mainly the loss of the aerodynamic damping of the wing modes due to the angle-of-attack changes during the motion. Figure 7 shows the influence of the more complete theoretical model for the blade aerodynamics, compared with the results using only the c_{ℓ_α} terms. The basic behavior remains the same, but the better aerodynamic model reduces slightly the level of the predicted damping ratio. The predicted speed at the stability boundary is significantly reduced, however, because of the gradual variation of the damping with speed. It is therefore concluded that for the prediction of the characteristics of an actual aircraft, the best model available for the rotor aerodynamics should be used.

Figure 8 shows the variation of the dynamic stability with velocity at the normal rotor speed ($\Omega = 458$ rpm), in terms of the frequency and damping ratio of the wing modes; the full-scale test results for the Bell rotor are compared with the predicted stability. Also shown are predictions from the Bell linear and nonlinear theories, from Reference 2. Figure 8 shows reasonable correlation between the predicted and full-scale test stability results. Additional comparisons with the full-scale test data are given in Reference 1.

Figure 9 shows the influence of the rotor lag motion. The predicted and measured stability is shown for the Bell rotor on the full-stiffness wing, and on a quarter-stiffness wing. (By operating on a quarter-stiffness wing at one-half design rotor speed, $\Omega = 229$ rpm, the wing frequencies and inflow ratio are modeled for an equivalent speed twice the actual tunnel speed.) Also shown is the predicted stability for the rotor on the full-stiffness wing, but without the ζ_{1c} and ζ_{1s} degrees of freedom. Figure 9a shows the variation of the wing vertical bending mode damping. The full-scale experimental data show a definite trend to higher damping levels with the full-stiffness wing, and this trend correlates well with the results of the present theory. Figures 9b and 9c show the predicted stability of all the wing modes. The difference in damping at the same inflow ratio is due to the rotor lag motion. Figure 9d shows the frequencies of the $\zeta - 1$, q_1, and p modes for the full-stiffness and quarter-stiffness wings. The full-stiffness wing has a resonance of the $\zeta - 1$ and q_1 modes which produces the peak in the damping. Slowing the rotor on the quarter-stiffness wing greatly increases the lag frequency (per rev), removing it from resonance with the q_1 mode. Another way to remove the influence of the rotor lag motion, in the theory, is simply to drop the ζ_{1c} and ζ_{1s} degrees of freedom from the full-stiffness wing case. When these degrees of freedom are dropped, the predicted wing vertical bending damping is almost identical to that for the quarter-stiffness wing (figs. 9a and 9b). Figure 10 examines further the influence of the rotor lag motion on the wing vertical bending mode damping. Predicted stability with and without the ζ_{1c} and ζ_{1s} degrees of freedom is compared with experimental results from tests of a 0.1333-scale model of a

gimballed, stiff-inplane proprotor. The test results are from Reference 6; this rotor is a model of the Bell M266, similar in design to the full-scale rotor considered here. The experimental data correlates well with the predictions, including the influence of the rotor lag motion.

Hingeless, Soft-Inplane Rotor

The effects of several elements of the theoretical model will be examined for a hingeless, soft-inplane rotor (the Boeing rotor). Then the theoretical results will be compared with the results of full-scale tests, and with results from the Boeing theory (the latter are from Reference 3). The predicted variation of the system stability with forward velocity at normal rotor speed ($\Omega = 386$ rpm) is shown in figure 11. The low-frequency flap ($\beta - 1$) mode becomes unstable at 480 knots. By the time this instability occurs, the mode has assumed the character of a wing vertical bending mode (i.e., the q_1 motion, and the associated p, ζ_{1c}, ζ_{1s}, and ζ_0 motions); hence this instability has the same mechanism as does the Bell rotor. With the soft-inplane rotor, $\nu_\zeta < 1$/rev, the proximity of the $\zeta - 1$ and q_1 mode frequencies significantly reduces the wing mode damping at low speeds; this effect is the air resonance phenomenon. A similar influence occurs with the resonance of the $\zeta - 1$ and q_2 modes, leading to an instability of the wing chord mode (this instability can occur because the wing chord mode aerodynamic damping remains low even at high speed). At higher Ω, this q_2 mode instability is, in fact, the critical instability. The influence of the rotor lag motion is shown in figure 12. The substantial decrease in the damping of the wing vertical and chordwise bending modes due to the rotor lag motion is the air resonance effect. Figure 13 shows the influence of powered operation and of omitting the wing aerodynamics, and figure 14 shows the influence of the better theoretical model for the rotor aerodynamics on the predicted stability. The effects, and hence the conclusions from figures 13 and 14 are similar to those for the Bell rotor.

Figure 15 shows the variation of the predicted stability of the Boeing rotor with rotor speed at 50 knots. At this low speed, the resonance of the $\zeta - 1$ and q_1 mode frequencies actually results in an instability of the wing vertical bending mode. Figure 16 shows the stability variation with rotor speed at 192 knots. The reduction in wing vertical bending mode damping due to air resonance is still present, but the increase in the rotor lag aerodynamic damping and wing vertical bending aerodynamic damping with flight speed has been sufficient to stabilize the motion even at resonance. Figure 17 summarizes the air resonance behavior of the Boeing rotor.

Figure 18 compares the predicted and full-scale results for the stability of the wing modes for a velocity sweep of the Boeing rotor at $\Omega = 386$ rpm. Figure 19 shows the variation of the wing vertical bending mode damping with rotor speed at $V = 50$ to 192 knots. These runs were conducted to investigate the air resonance behavior of this configuration, i.e., the influence of the rotor lag motion. Reasonable correlation is shown between the predicted and measured stability, except at the higher speeds where tunnel turbulence made extraction of the damping ratio from the experimental transient wing motion difficult. Also shown are predictions from the Boeing theory, from Reference 3. Additional comparisons with the full-scale test data are given in Reference 1.

Concluding Remarks

This paper has presented theoretical results for the stability of a proprotor operating in high inflow on a cantilever wing. Some experimental results from full-scale tests have been presented, showing reasonable correlation with the predicted stability. The nine degrees-of-freedom theoretical model has been established as a useful and accurate representation of the basic dynamic characteristics of the proprotor and cantilever wing system. The significant influence of the rotor speed perturbation degree of freedom (i.e., windmilling or powered operation), the wing aerodynamics, and the rotor aerodynamic model on the predicted stability have been shown, indicating the importance of including these elements accurately in the theoretical model. From a comparison of the behavior of the gimballed, stiff-inplane rotor and the hingeless, soft-inplane rotor, it is concluded that the placement of the natural frequencies of the rotor blade first mode bending — i.e., the flap frequency ν_β and the lag frequency ν_ζ — has a great influence on the dynamics of the proprotor and wing. Moreover, the theoretical and experimental results have demonstrated that the rotor lag degree of freedom has a very important role in the proprotor dynamics, for both the soft-inplane ($\nu_\zeta < 1$/rev) and stiff-inplane ($\nu_\zeta > 1$/rev) configurations.

References

1. NASA TN-D (in preparation), THE DYNAMICS OF TILTING PROPROTOR AIRCRAFT IN CRUISE FLIGHT, Johnson, Wayne, 1974.

2. NASA CR 114363, ADVANCEMENT OF PROPROTOR TECHNOLOGY TASK II — WIND TUNNEL TEST RESULTS, Bell Helicopter Company, September 1971.

3. Boeing Vertol Company Report No. D222-10059-1, WIND TUNNEL TESTS OF A FULL SCALE HINGELESS PROP—ROTOR DESIGNED FOR THE BOEING MODEL 222 TILT ROTOR AIRCRAFT, Magee, John P., and Alexander, H. R., July 1973.

4. NASA CR 114442, V/STOL TILT—ROTOR STUDY TASK II — RESEARCH AIRCRAFT DESIGN, Bell Helicopter Company, March 1972.

5. NASA CR 114438, V/STOL TILT—ROTOR AIRCRAFT STUDY VOLUME II — PRELIMINARY DESIGN OF RESEARCH AIRCRAFT, Boeing Vertol Company, March 1972.

6. Kvaternik, Raymond G., STUDIES IN TILT—ROTOR VTOL AIRCRAFT AEROELASTICITY, Ph.D. Thesis, Case Western Reserve University, June 1973.

TABLE I — DESCRIPTION OF THE FULL–SCALE PROPROTORS, AS TESTED IN THE AMES 40- BY 80-FT WIND TUNNEL.

	Bell	Boeing
Rotor		
Type	gimballed, stiff-inplane	hingeless, soft-inplane
Number of blades	3	3
Radius, R	3.81 m (12.5 ft)	3.96 m (13 ft)
Lock number, γ	3.83	4.04
Solidity ratio	0.089	0.115
Pitch/flap coupling, δ_3	-15 deg	0
Rotor rotation direction, on right wing	clockwise	counterclockwise
Tip speed, ΩR (cruise mode)	183 m/sec (600 ft/sec)	160 m/sec (525 ft/sec)
Rotation speed, (cruise mode)	458 rpm	386 rpm
Wing		
Semispan, y_w/R	1.333	1.281
Mast height, h/R	0.342	0.354

Typical frequencies				
Vertical bending	3.2 Hz	0.42/rev	2.3 Hz	0.36/rev
Chordwise bending	5.35	0.70	4.0	0.62
Torsion	9.95	1.30	9.2	1.48

Figure 2. Blade rotating natural frequencies for the Bell rotor. (a) flap frequency ν_β (normal $\Omega = 458$ rpm), (b) lag frequency ν_ζ (V/ΩR = 1 at 355 knots and normal Ω).
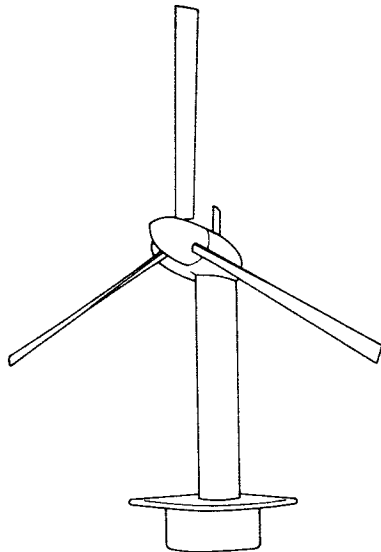
Figure 1. Configuration of analytical model, and for full-scale tests: proprotor operating in high inflow axial flight on a cantilever wing.
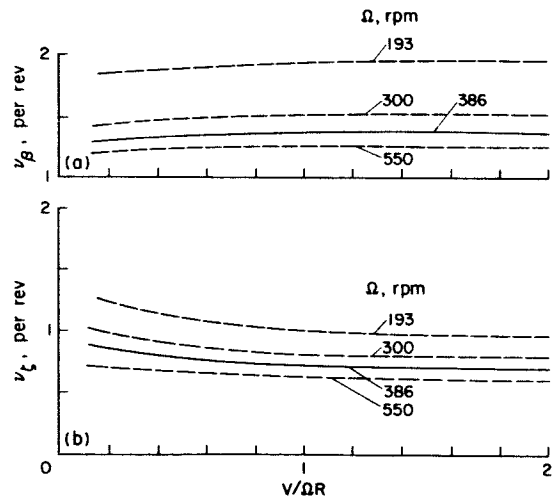
Figure 3. Blade rotating natural frequencies for the Boeing rotor (V/ΩR = 1 at 311 knots and normal Ω, 386 rpm). (a) flap frequency ν_β, (b) lag frequency ν_ζ.

Figure 5. Effect of deleting the rotor lag degrees of freedom (ζ_{1c} and ζ_{1s}), Bell rotor velocity sweep at $\Omega = 458$ rpm. (a) damping of wing vertical bending mode (q_1), (b) damping of chordwise bending (q_2) and torsion (p) modes.
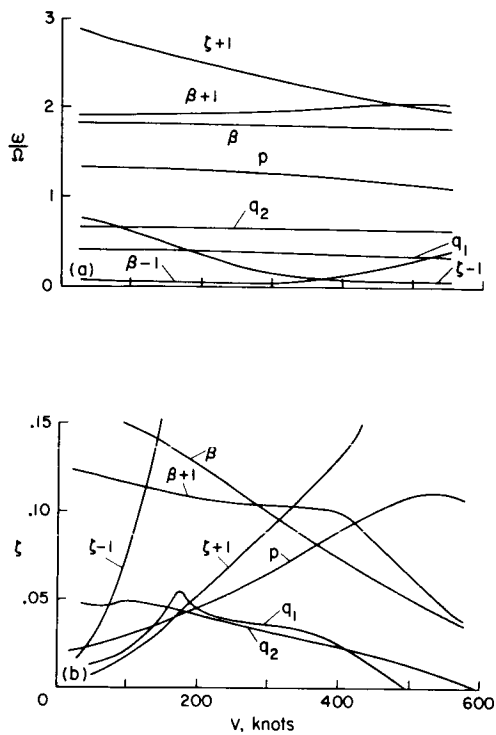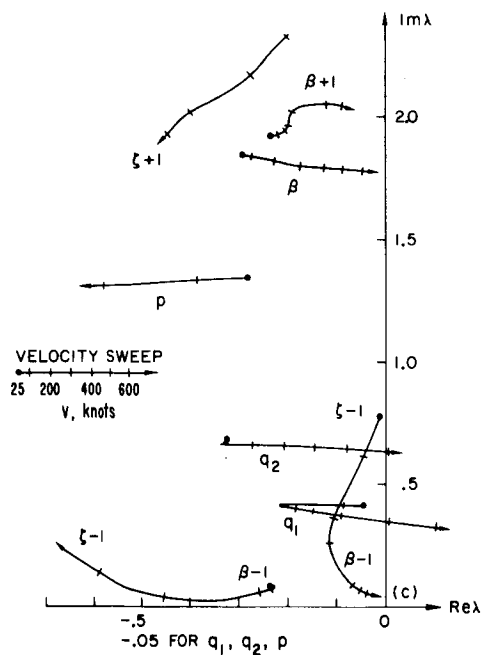

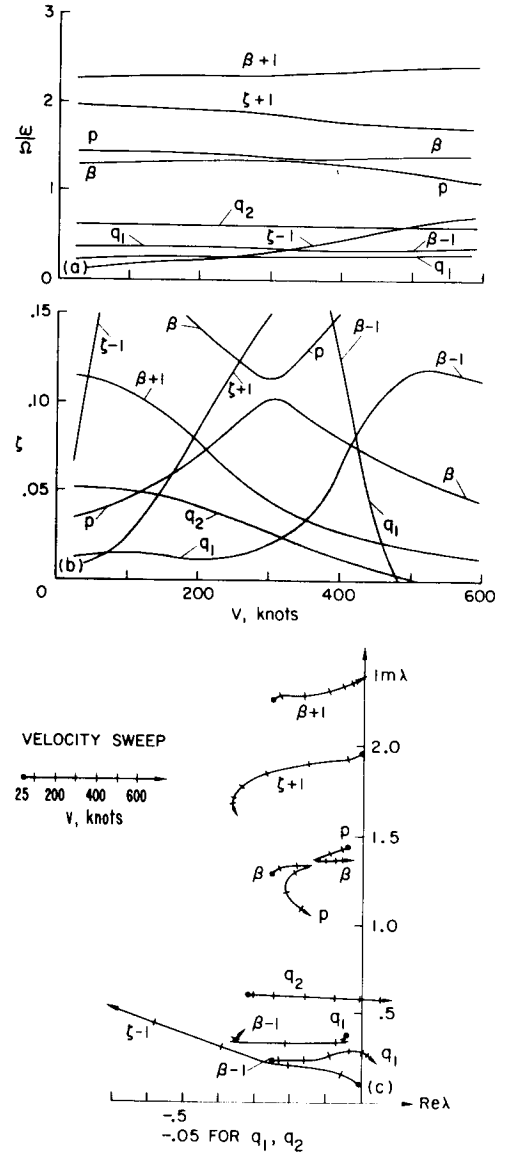Figure 4. Predicted stability of Bell rotor, velocity sweep at $\Omega = 458$ rpm. (a) frequency of the modes, (b) damping ratio of the modes, (c) root locus.
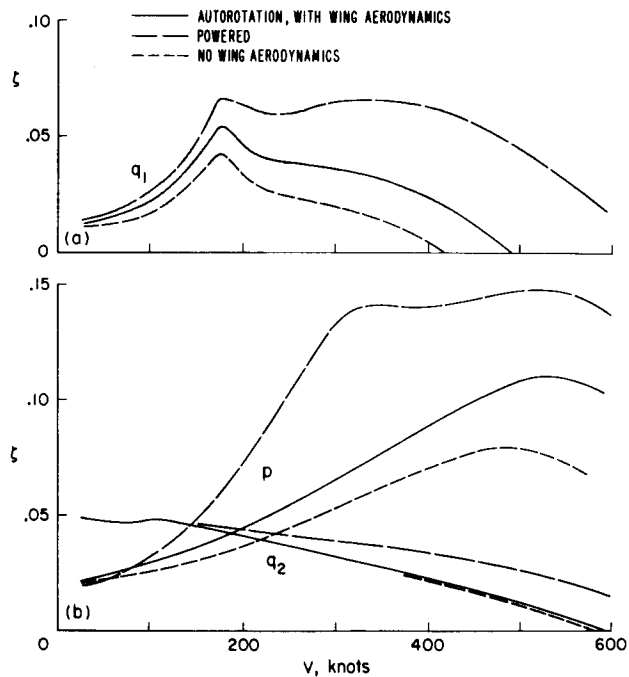
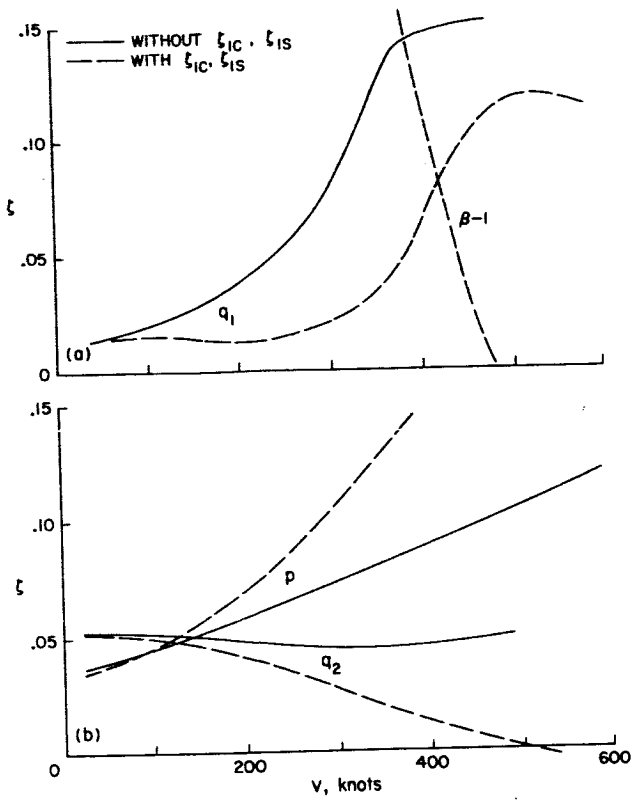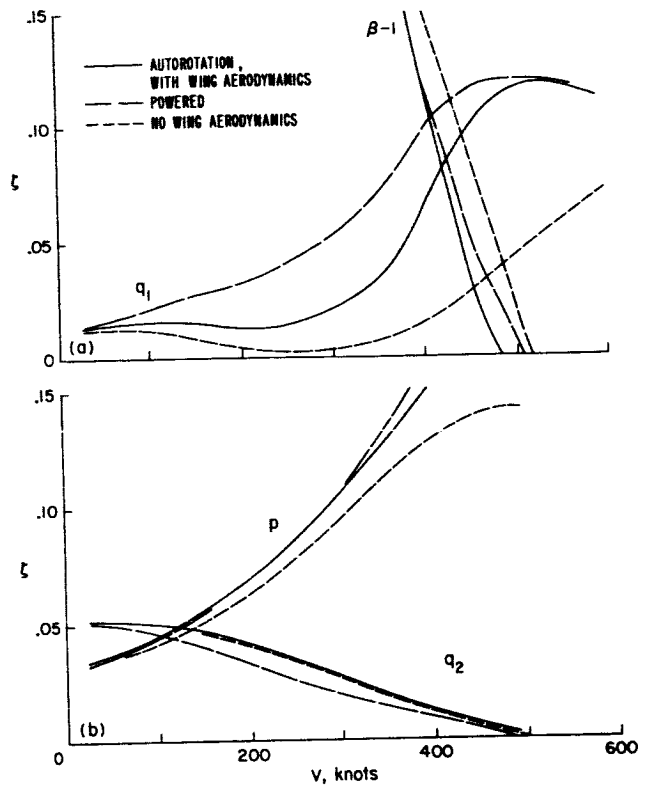Figure 6. Influence of powered operation, and wing aerodynamic forces, Bell rotor velocity sweep at $\Omega = 458$ rpm. (a) damping of wing vertical bending mode (q_1), (b) damping of chordwise bending (q_2) and torsion (p) modes.

164
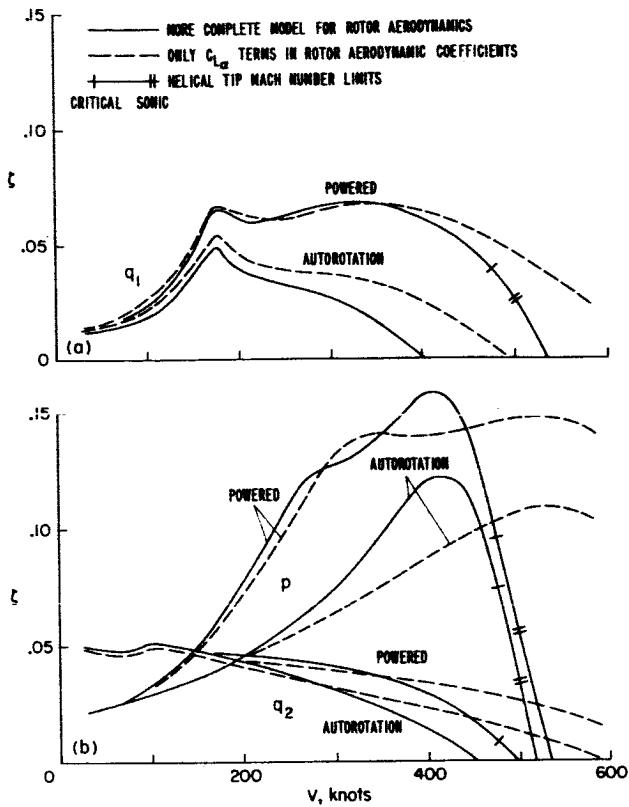
Figure 7. Influence of a more complete model for the rotor
aerodynamics, Bell rotor velocity sweep at $\Omega = 458$ rpm.
(a) damping of wing vertical bending mode (q_1),
(b) damping of chordwise bending (q_2) and torsion (p)
modes.
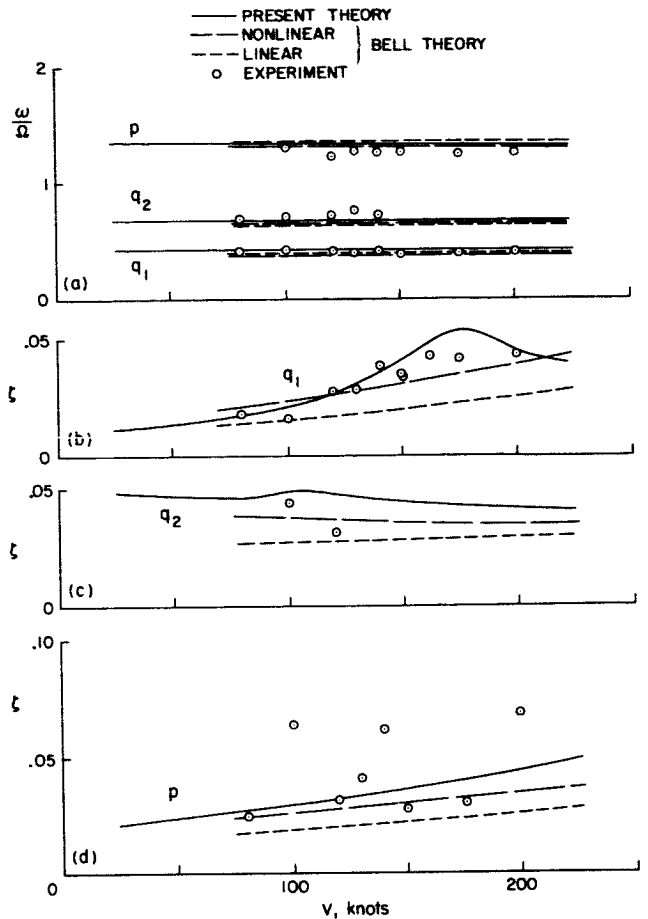
Figure 8. Comparison with full-scale experimental data, Bell
rotor velocity sweep at $\Omega = 458$ rpm. (a) frequency of the
modes, (b) damping of the wing vertical bending mode (q_1),
(c) damping of wing chordwise bending mode (q_2),
(d) damping of wing torsion mode (p).
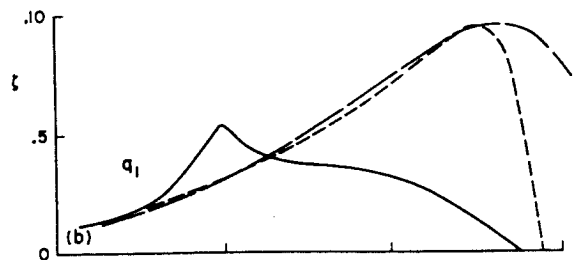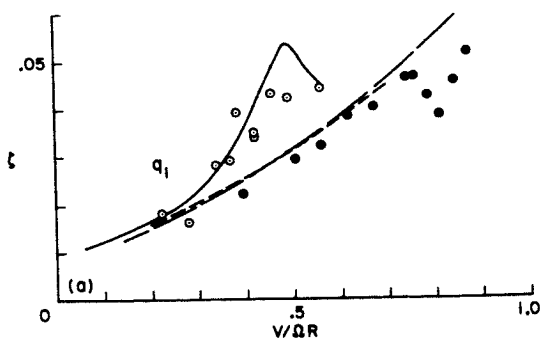
Figure 9. Influence of the rotor lag motion, Bell rotor velocity sweeps on the full-stiffness wing, on a quarter-stiffness wing, and on
the full-stiffness wing without the ζ_{1c} and ζ_{1s} degrees of freedom (theory only). (a) damping of the wing vertical bending
mode (q_1), comparison with full-scale experimental data, (b) damping of wing vertical bending mode (q_1), (c) damping of wing
chordwise bending (q_2) and torsion (p) modes, (d) frequency of the modes.

165
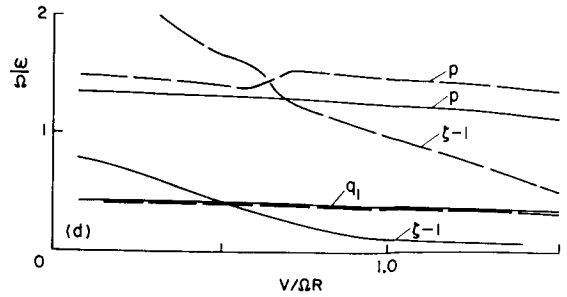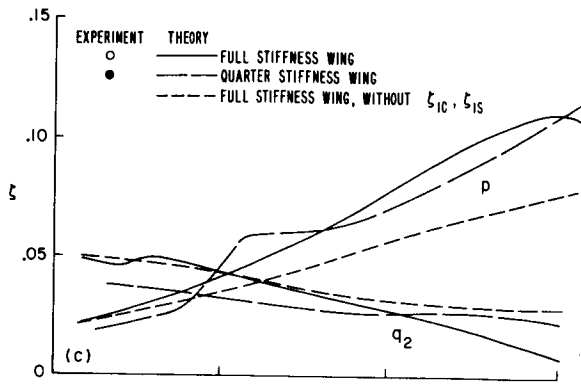
Figure 9. Concluded.
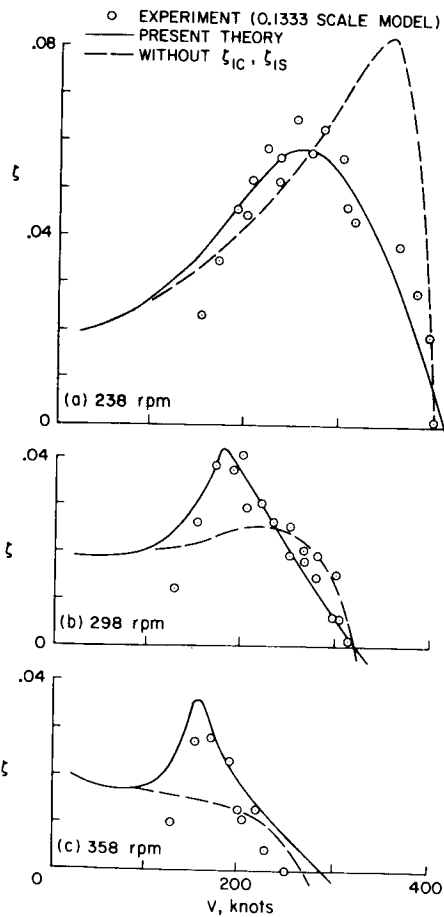
Figure 10. Comparison with experimental data from tests of a 0.1333-scale rotor and cantilever wing model of Bell M266 aircraft (experimental points from Reference 6), velocity sweeps at (a) $\Omega = 238$ rpm, (b) $\Omega = 298$ rpm, (c) $\Omega = 358$ rpm (equivalent full-scale V and Ω).

Figure 11. Predicted stability of Boeing rotor, velocity sweep at $\Omega = 386$ rpm. (a) frequency of the modes, (b) damping ratio of the modes, (c) root locus.

166

Figure 12. Effect of deleting the rotor lag degree of freedom (ζ_{1c} and ζ_{1s}), Boeing rotor velocity sweep at $\Omega = 386$ rpm (a) damping of wing vertical bending (q_1) and flap ($\beta - 1$) modes (the $\beta - 1$ mode is shifted by 250-300 knots to higher speed by the removal of the lag influence, beyond the scale shown), (b) damping of wing chordwise bending (q_2) and torsion (p) modes.

Figure 13. Influence of powered operation, and wing aerodynamic forces, Boeing rotor velocity sweep at $\Omega = 386$ rpm. (a) damping of wing vertical bending (q_1) and rotor flap ($\beta - 1$) modes, (b) damping of wing chordwise bending (q_2) and torsion (p) modes.
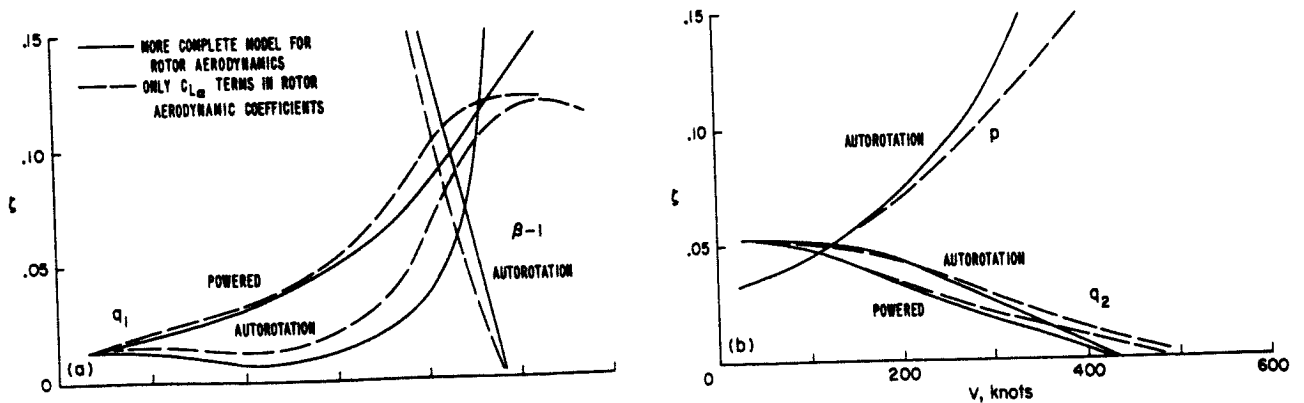
Figure 14. Influence of a more complete model for the rotor aerodynamics. Boeing rotor velocity sweep at $\Omega = 386$ rpm (a) damping of wing vertical bending (q_1) and rotor flap ($\beta - 1$) modes, (b) damping of wing chordwise bending (q_2) and torsion (p) modes.
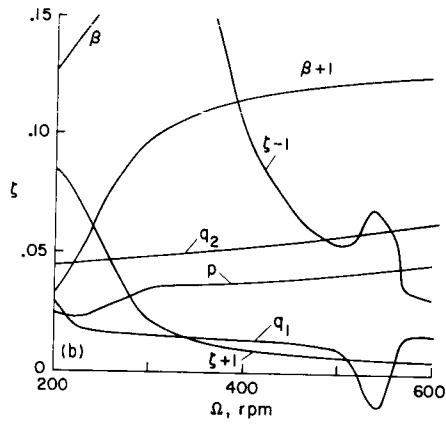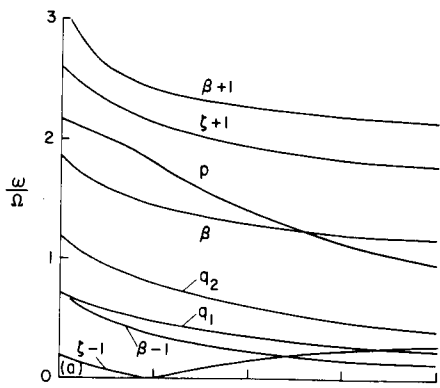
167

Figure 15. Predicted stability of Boeing rotor, rpm sweep at 50 knots. (a) frequency of the modes, (b) damping ratio of the modes.
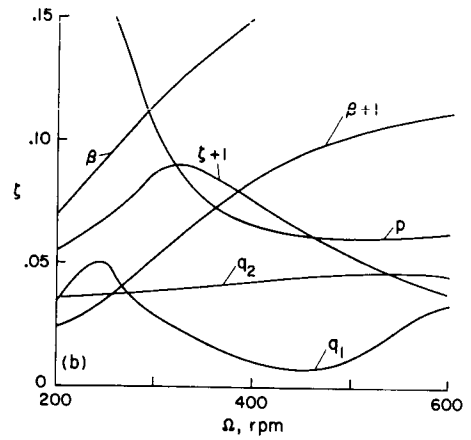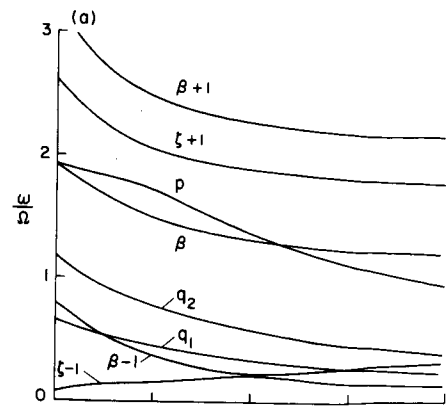
Figure 16. Predicted stability of Boeing rotor, rpm sweep at 192 knots. (a) frequency of the modes, (b) damping ratio of the modes.
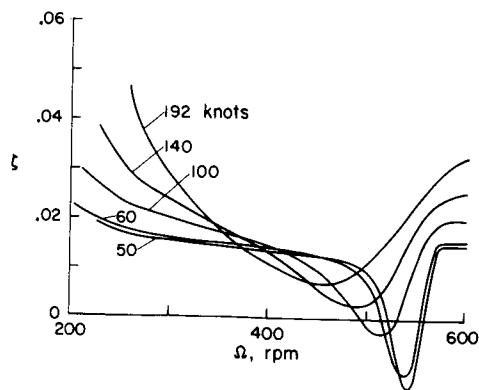

Figure 17. Air resonance behavior of soft-inplane hingeless rotor. Boeing rotor at 50 to 192 knots, variation of damping of wing vertical bending mode (q_1) with rotor speed.
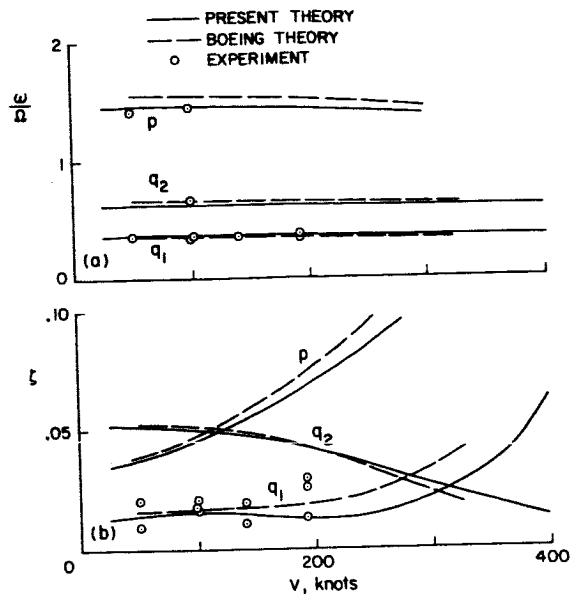
Figure 18. Comparison with full-scale experimental data, Boeing rotor velocity sweep at $\Omega = 386$ rpm. (a) frequency of the modes, (b) damping of the wing vertical bending (q_1), chord bending (q_2), and torsion (p) modes; the experimental data is for q_1 only.
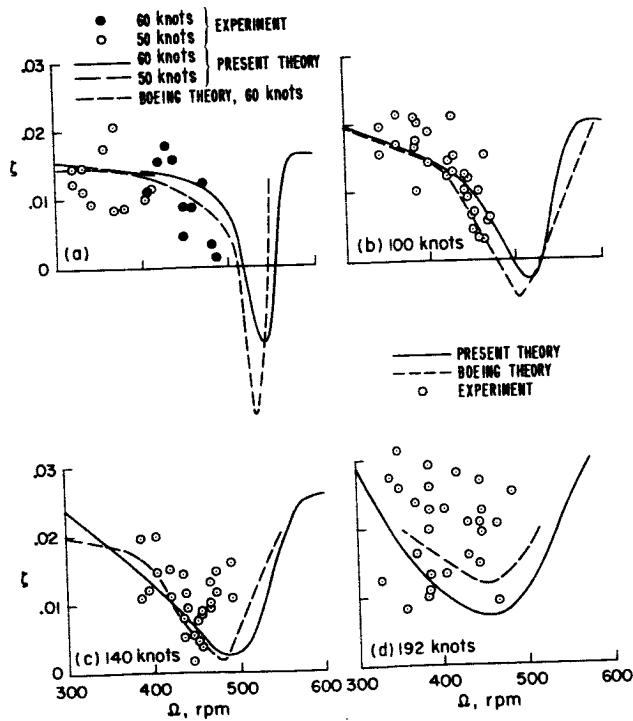

Figure 19. Comparison with full-scale experimental data, Boeing rotor rpm sweeps, damping of wing vertical bending mode at (a) 50-60 knots, (b) 100 knots, (c) 140 knots, (d) 192 knots.

169